FREQUENCY DOMAIN REVERSE TIME MIGRATION FOR ACOUSTIC-ELASTIC COUPLED MEDIA USING THE WAVEFIELD SEPARATION METHOD

SEUNG-GOO KANG[1], WANSOO HA[2], CHANGSOO SHIN[3], JONG KUK HONG[1] and YOUNG KEUN JIN[1]

[1] Division of Polar Earth-System Sciences, Korea Polar Research Institute, KIOST, Incheon 406-840, South Korea.
[2] Department of Energy Resources Engineering, Pukyong National University, Busan 608-737, South Korea. wansooha@gmail.com
[3] Department of Energy Systems Engineering, Seoul National University, Seoul 151-742, South Korea.

ABSTRACT

Kang, S.-G., Ha, W., Shin, C., Hong, J.K. and Jin, Y.K., 2016. Frequency domain reverse time migration for acoustic-elastic coupled media using the wavefield separation method. *Journal of Seismic Exploration*, 25: 57-85.

　　Recent research results concerning frequency domain reverse time migration based on the adjoint-state of the acoustic wave equation have highlighted several limitations imposed by the use of an acoustic-based algorithm. In marine seismic exploration, targeted areas are located within elastic media. Elastic wave components, such as S-waves, surface waves and mode converted waves can remain obscured by reverse time migration based on the acoustic wave equation in the targeted media. Several research papers addressing the topic of acoustic-elastic coupled media with full waveform inversion have shown that this method can generate more accurate inversion results for P-wave velocity models than acoustic-based algorithms. This paper formulates the frequency domain reverse time migration for acoustic-elastic coupled media based on the adjoint-state of the wave equation. It goes on to adopt the wavefield separation method to reduce the effects of crosstalk artifacts on migrated images. The validity of the proposed algorithm is demonstrated using a synthetic dataset generated by elastic staggered grid time modeling. The image of the frequency domain reverse time migration for acoustic-elastic coupled media calculated using the wavefield separation method is then compared to the results of the acoustic reverse time migration and reverse time migration for acoustic-elastic coupled media using a conventional zero-lag cross-correlation approach. Comparison of the migration images revealed that the images of acoustic-elastic coupled media from the wavefield separation method resolved geological structures with greater accuracy and exhibited fewer noise-contaminated components than those obtained from the acoustic and conventional acoustic-elastic coupled media imaging methods. We also analyze the reverse time migration method's sensitivity to correct P- and S-wave inputs and density model assumptions.

KEY WORDS: frequency domain, reverse time migration, acoustic-elastic coupled media, adjoint-state wave equation, marine seismic data, wavefield separation.

INTRODUCTION

Migration methods are used in seismic data processing to obtain an accurate image of subsurface geologic structure. Migration involves the geometric repositioning of the return signals to detect where an event is being hit by seismic waves rather than where the feature was originally sensed. Seismic exploration is being applied to increasingly complex regions, which may contain steep reflectors or sudden seismic velocity variation. The structure in these regions requires further refinement of algorithms used to process and interpret seismic data. Reverse time migration algorithms that use two-way wave equations are appropriate for this application because they preserve the true amplitude of seismic data and deal with multi-path and steeply dipping structures (Whitmore, 1983; Baysal et al., 1983; McMechan, 1983; Loewenthal and Mufti, 1983; Shin et al., 2001, 2003; Plessix and Mulder, 2004; Xu et al., 2010; Kim et al., 2011; Lee et al., 2012). Shin et al. (2003) proposed reverse time migration in the frequency domain using the adjoint-state of the acoustic wave equation to improve computational efficiency. To enhance the resolution of the migrated image, Kim et al. (2011) proposed a source wavelet estimation method that was based on the full Newton method. Lee et al. (2012) introduced the frequency domain reverse time migration using the L_1-norm to minimize outlier effects on seismic data.

Previously, marine seismic data were processed using acoustic-based algorithms. As a result, elastic effects in marine seismic data, such as shear reflections, mode-converted waves and amplitude-offset variations, are neglected. Several lines of research regarding the wave propagation modeling and full waveform inversion of acoustic-elastic coupled media have been pursued to overcome the acoustic algorithm's limitations in dealing with elastic waves effects in marine survey data. Studies of acoustic-elastic coupled media have used continuity conditions for the normal stresses and components of particle velocity at the interface between acoustic and elastic media. Komatitsch et al. (2000) proposed a spectral element approach, Zienkiewicz et al. (2005) presented a finite element method and Lee et al. (2009) designed a displacement-based finite difference method for wave propagation modeling. Choi et al. (2008) and Kim et al. (2009) proposed the frequency domain full waveform inversion for acoustic-elastic coupled media using a finite element approach, and Bae et al. (2010) developed waveform inversion in the Laplace domain for acoustic-elastic coupled media. Kang et al. (2012) proposed the Laplace-Fourier domain full waveform inversion of acoustic-elastic coupled media. These authors demonstrated full waveform inversion for acoustic-elastic coupled media that used only the pressure field in marine seismic data. Their approach generated inverted P- and S-wave velocity and density models, including inverted P-wave velocity models superior to those generated by the acoustic approximation method.

In this study, we develop the frequency domain reverse time migration method for acoustic-elastic coupled media in order to evaluate elastic wave imaging of sub-marine geologic structure. We generate forward data for the reverse time migration by performing finite element wave propagation modeling for acoustic-elastic coupled media in the frequency domain. Next, we calculate migration images for acoustic-elastic coupled media in the frequency domain from zero-lag cross-correlation between the partial derivative wavefields of acoustic-elastic coupled media with respect to the P- and S-wave velocities and the observed seismic data. The migration images are effectively computed using the back-propagation algorithm (Lailly, 1983; Tarantola, 1984; Pratt et al., 1998). To eliminate crosstalk artifacts and noise in our migration images, we employ the wavefield separation method (Chung et al., 2012) to separate the pure P-wave migration image from the S-wave and other noise-contaminated components in an acoustic-elastic coupled system. Our migration algorithm uses the 2D isotropic elastic wave equation to describe the elastic effects of wave propagation in the subsurface.

We also perform numerical tests on synthetic datasets to verify the proposed reverse time migration algorithm. Modified elastic Hess and IFP/UH Marmousi-2 models generated data that mimicked the geometry of a marine survey using a time-domain staggered grid elastic modeling method (Symons et al., 2006; Virieux, 1986). We present three types of migration images and compare them in the Numerical Examples section below. A migrated seismic image from the reverse time migration for acoustic-elastic coupled media using the wavefield separation method is then compared with results of acoustic reverse time migration and migration images from the reverse time migration for acoustic-elastic coupled media using a conventional approach (without the wavefield separation method). We also generated a migration image from smoothed input models to evaluate the method's sensitivity to model inputs, namely their impact on the migration image from acoustic-elastic coupled media.

FORWARD MODELING OF ACOUSTIC-ELASTIC COUPLED MEDIA USING THE FINITE ELEMENT METHOD IN THE FREQUENCY DOMAIN

For 2D marine seismic exploration, survey targets lie beneath the seafloor. Fig. 1 shows a simple diagram of wave propagation for 2D seismic surveys. In acoustic-elastic coupled media, wave propagation in the water column occurs as longitudinal pressure variation, which is best described by the acoustic wave equation. Wave propagation beneath the seafloor occurs as particle displacements, which are best described by the isotropic elastic wave equation. We applied wave propagation modeling for acoustic-elastic coupled media using the finite element method to generate forward data for frequency domain reverse time migration.
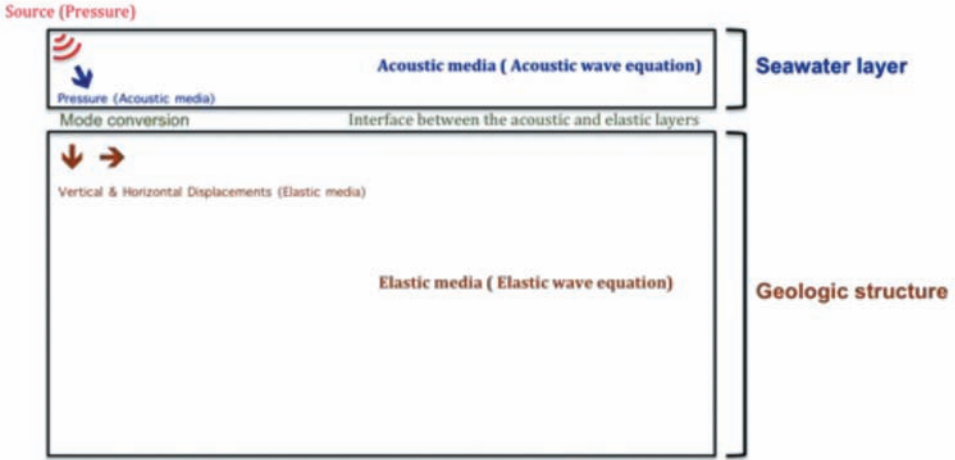
Fig. 1. Diagram of the two-dimensional acoustic-elastic coupled media.

The Fourier-transformed acoustic wave equation is defined as follows:

$$-(\omega^2/c^2)\tilde{p} = (\partial^2\tilde{p}/\partial x^2) + (\partial^2\tilde{p}/\partial z^2) + \tilde{f} \ , \tag{1}$$

where ω is the angular frequency, $\tilde{p}(x,z,\omega)$ is the Fourier-transformed pressure field in acoustic media, $c(x,z)$ is the P-wave velocity in the acoustic medium and $\tilde{f}$ is the source term.

For elastic media, the wave equation in the frequency domain can be expressed as

$$-\rho_E\omega^2\tilde{h} = (\partial/\partial x)[(\lambda + 2\mu)(\partial\tilde{h}/\partial x) + \lambda(\partial\tilde{v}/\partial z)]$$

$$+ (\partial/\partial z)\{\mu[(\partial\tilde{v}/\partial x) + (\partial\tilde{h}/\partial z)]\} \ ,$$

$$-\rho_E\omega^2\tilde{v} = (\partial/\partial x)\{\mu[(\partial\tilde{v}/\partial x) + (\partial\tilde{h}/\partial z)]\} \tag{2}$$

$$+ (\partial/\partial z)[\lambda(\partial\tilde{h}/\partial x) + (\lambda + 2\mu)(\partial\tilde{v}/\partial z)] \ ,$$

where $\rho_E(x,z)$ is the density, $\lambda(x,z)$ and $\mu(x,z)$ are the Lamé parameters and $\tilde{h}(x,z,\omega)$ and $\tilde{v}(x,z,\omega)$ are the Fourier-transformed horizontal and vertical displacements, respectively.

At the interface between acoustic and elastic media, the continuity condition for the normal component of particle velocity (Zienkiewicz et al., 2005) is

$$\nabla \tilde{p} \cdot \mathbf{n} = \rho_A (\tilde{h}'', \tilde{v}'') \cdot \mathbf{n} \quad , \tag{3}$$

where $\mathbf{n}$ is the unit normal vector from the interface, $(\tilde{h}'', \tilde{v}'')$ denotes the second derivatives of the horizontal and vertical displacements and $\rho_A(x,z)$ is the density of the acoustic media. The stress continuity condition (Komatitsch et al., 2000) can be expressed as

$$\sigma \cdot \mathbf{n} = -\tilde{p} \cdot \mathbf{n} \quad , \tag{4}$$

where σ is the symmetric second-order stress tensor.

The Fourier-transformed wave equations and continuity condition for acoustic-elastic coupled media are expressed in a matrix formulation with stiffness and mass matrices of acoustic and elastic wave equations using the finite element method as follows (Choi et al., 2008):

$$\begin{pmatrix} \mathbf{K}^A + \omega^2/c^2 \, \mathbf{M}^A & \rho_A \omega^2 \mathbf{Q}^A & \rho_A \omega^2 \mathbf{Q}^A \\ \left[\mathbf{Q}^E\right]^T & \mathbf{K}^{11} - \rho_E \omega^2 \mathbf{M}^{11} & \mathbf{K}^{12} \\ \left[\mathbf{Q}^E\right]^T & \mathbf{K}^{21} & \mathbf{K}^{22} - \rho_E \omega^2 \mathbf{M}^{22} \end{pmatrix} \begin{pmatrix} \tilde{p} \\ \tilde{h} \\ \tilde{v} \end{pmatrix} = \begin{pmatrix} \tilde{f} \\ 0 \\ 0 \end{pmatrix} , \tag{5}$$

where $\mathbf{K}^A$ denotes a stiffness matrix for acoustic media, $\mathbf{K}^{11}$, $\mathbf{K}^{12}$, $\mathbf{K}^{21}$ and $\mathbf{K}^{22}$ indicate the stiffness matrices for elastic media, $\mathbf{M}^A$ designates a mass matrix for acoustic media, $\mathbf{M}^{11}$ and $\mathbf{M}^{22}$ are the mass matrices for elastic media and $\mathbf{Q}^A$ and $\mathbf{Q}^E$ represent the interface boundary matrices in the respective acoustic and elastic media. The term $\tilde{p}$ is the frequency domain pressure field vector, $\tilde{h}$ and $\tilde{v}$ are Fourier-transformed horizontal and vertical displacements (respectively) in vector form for elastic media, and $\tilde{f}$ indicates the source vector (pressure field), which is generated by an air-gun at the upper surface of the water column.

We simplify eq. (5) using the complex impedance matrix $\mathbf{S}$ by the finite element method for acoustic-elastic coupled media:

$$\mathbf{S}\tilde{u} = \tilde{f} \quad , \tag{6}$$

where $\tilde{u}$ represents frequency domain wavefields for acoustic-elastic coupled media, which consist of pressure fields and the vertical and horizontal displacements. We apply a perfectly matched layer (PML) boundary condition (Cohen, 2002) to eliminate reflection events from the left, right and bottom of the model's boundaries.

REVERSE TIME MIGRATION FOR ACOUSTIC-ELASTIC COUPLED MEDIA

For acoustic-elastic coupled media, reverse time migration can be defined as a zero-lag cross-correlation between the partial-derivative wavefields of the elastic parameters of acoustic-elastic coupled media and the seismic data in the time domain (Shin et al., 2003):

$$\psi_k = \sum_{s=1}^{Nshot} \int_0^{T_{max}} \{[\partial \mathbf{u}_s(t)/\partial m_{E_k}]^T \mathbf{d}_s(t)\} dt \quad , \tag{7}$$

where ψ_k is the migration image for the k-th model parameter, s is the shot index, Nshot is the total number of shots, T_{max} is the maximum recording time, $\mathbf{u}_s(t)$ is the forward modeled wavefield vector, m is the k-th elastic model parameter in acoustic-elastic coupled media (P- and S-wave velocities and the density), $\partial \mathbf{u}_s(t)/\partial m$ is the partial derivative of the wavefield vector of coupled media that is related to the k-th elastic model parameter m_k and $\mathbf{d}_s(t)$ is the observed wavefield vector. The superscript T indicates the transpose of the vector.

This migration method calculates a migration image for acoustic-elastic coupled media in the frequency domain using the Fourier-transform of eq. (7):

$$\psi_k = \sum_{s=1}^{Nshot} \int_0^{\omega_{max}} Re\{[\partial \tilde{\mathbf{u}}_s(\omega)/\partial m_{E_k}]^T \tilde{\mathbf{d}}_s^*(\omega)\} d\omega \quad , \tag{8}$$

where $\tilde{\mathbf{u}}_s(\omega)$ is a forward modeled data vector in the frequency domain, $\tilde{\mathbf{d}}_s^*(\omega)$ is the Fourier-transformed observed seismic data vector and Re is the real part of the complex value. The superscript * denotes the complex conjugate.

The partial derivative wavefield of acoustic-elastic coupled media can be calculated by the derivative of eq. (6) with respect to the elastic model parameter m as follows (Pratt et al., 1998):

$$S[\partial \tilde{\mathbf{u}}_s(\omega)/\partial m_{E_k}] + [\partial S/\partial m_{E_k}]\tilde{\mathbf{u}}_s(\omega) = 0 \quad , \tag{9}$$

and

$$\partial \tilde{\mathbf{u}}_s(\omega)/\partial m_{E_k} = S^{-1}\mathbf{f}_v \quad , \tag{10}$$

where $\mathbf{f}_v = -(\partial S/\partial m_{E_k})\tilde{\mathbf{u}}_s(\omega)$ is the virtual source vector of acoustic-elastic coupled media for the k-th set of elastic model parameters. Thus, the imaging condition of reverse time migration in the frequency domain can be rewritten as the cross-correlation between the virtual source and the back-propagated

observed seismic data as follows (Pratt et al., 1998; Shin et al., 2003):

$$\psi_k = \sum_{s=1}^{Nshot} \int_0^{\omega_{max}} Re\{f_v^T(S^T)^{-1}\tilde{d}_s^*(\omega)\}d\omega \quad . \tag{11}$$

We calculate the virtual sources of acoustic-elastic coupled media with respect to the P- and S-wave velocities because they represent the most pertinent elastic model parameters (Chung et al., 2012):

$$\mathbf{f}_{vp} = -(\partial S/\partial Vp_k)\tilde{u}_s \quad , \tag{12}$$

and

$$\mathbf{f}_{vs} = -(\partial S/\partial Vs_k)\tilde{u}_s \quad , \tag{13}$$

where f_{vp} and f_{vs} are the virtual source vectors of the P- and S-wave velocities, respectively.

We can calculate the P- and S-wave migration images of acoustic-elastic coupled media using the respective virtual source vectors as follows:

$$[\psi_k]_p = \sum_{s=1}^{Nshot} \int_0^{\omega_{max}} Re\{f_{vp}^T(S^T)^{-1}\tilde{d}_s^*(\omega)\}d\omega \quad , \tag{14}$$

and

$$[\psi_k]_s = \sum_{s=1}^{Nshot} \int_0^{\omega_{max}} Re\{f_{vs}^T(S^T)^{-1}\tilde{d}_s^*(\omega)\}d\omega \quad , \tag{15}$$

where $[\psi_k]_p$ and $[\psi_k]_s$ are the respective P- and S-wave migration images for the acoustic-elastic coupled media.

The inverse of the pseudo Hessian matrix (Shin et al., 2001) can compensate the imaging value of reverse time migration by multiplying the imaging condition terms.

$$[\psi]_p = \int_0^{\omega_{max}} \left[\sum_{s=1}^{Nshot} Re\{F_{vp}^T(S^T)^{-1}\tilde{d}_s^*(\omega)\} / [\sum_{s=1}^{Nshot} Diag\{F_{vp}^T F_{vp}\} + \chi] \right]d\omega \quad , \tag{16}$$

and

$$[\psi]_s = \int_0^{\omega_{max}} \left[\sum_{s=1}^{Nshot} Re\{F_{vs}^T(S^T)^{-1}\tilde{d}_s^*(\omega)\} / [\sum_{s=1}^{Nshot} Diag\{F_{vs}^T F_{vs}\} + \chi] \right]d\omega \quad , \tag{17}$$

where $\mathbf{F}_{vp}$ and $\mathbf{F}_{vs}$ are the virtual source matrices, which consist of the virtual source vectors $\mathbf{f}_{vp}$ and $\mathbf{f}_{vs}$ at all grid points, respectively. $\text{Diag}\{\mathbf{F}_{vs}^{T}\mathbf{F}_{vs}\}$ is the diagonal elements of the pseudo-Hessian matrix, and χ is a damping factor (Shin et al., 2001).

We can calculate P- and S-wave migrated images for acoustic-elastic coupled media from marine seismic data by imaging conditions in eqs. (16) and (17). Migrated images based on the 2-D isotropic elastic wave equation may not resolve detailed geological structures however, because they contain crosstalk artifacts. We adopt the wave separation method for acoustic-elastic coupled media to reduce crosstalk effects in the elastic media. Chung et al. (2012) proposed the wavefield separation method for elastic reverse time migration. This method calculates elastic migration images by zero-lag correlation between the decomposed virtual source and the decomposed backpropagated potential wavefields using divergence and curl operators. Chung et al.'s (2012) approach generates better images than those generated by conventional zero-lag cross-correlation methods. Similar to elastic migration, our migration algorithm calculates the P- and S-wave migration images using zero-lag cross-correlation between the virtual source and back-propagated wavefield. Following the wavefield separation method of Chung et al. (2012), we can rewrite the final migration step applied to acoustic-elastic coupled media using the divergence and curl operations as follows:

$$[\psi]_p = \int_0^{\omega_{max}} \Big[\sum_{s=1}^{Nshot} \text{Re}\{(\nabla\cdot\mathbf{F}_{vp})^{T}[\nabla\cdot(\mathbf{S}^{T})^{-1}\tilde{\mathbf{d}}_s^*(\omega)]\}$$
$$/ \: [\sum_{s=1}^{Nshot} \text{Diag}\{(\nabla\cdot\mathbf{F}_{vp})^{T}(\nabla\cdot\mathbf{F}_{vp}\} + \chi]\Big]d\omega \quad, \tag{18}$$

and

$$[\psi]_s = \int_0^{\omega_{max}} \Big[\sum_{s=1}^{Nshot} \text{Re}\{(\nabla\times\mathbf{F}_{vs})^{T}[\nabla\times(\mathbf{S}^{T})^{-1}\tilde{\mathbf{d}}_s^*(\omega)]\}$$
$$/ \: [\sum_{s=1}^{Nshot} \text{Diag}\{(\nabla\times\mathbf{F}_{vs})^{T}(\nabla\times\mathbf{F}_{vs}\} + \chi]\Big]d\omega \quad. \tag{19}$$

We thus obtain fully separated migration images of the P- and S-wave velocities for acoustic-elastic coupled media.

NUMERICAL EXAMPLES

In this section, we demonstrate our proposed migration algorithm using the Hess and IFP/UH Marmousi-2 models. First, we compare the frequency domain reverse time migration for acoustic-elastic coupled media and the wavefield separation method with acoustic reverse time migration based on the Hess model. To generate synthetic data, we employ elastic 2D staggered grid time modeling using the first-order elastic wave equation (Symons et al., 2006; Virieux, 1986). We modify the original elastic Hess models by including an overlying water column of 400 m depth for a reverse time migration evaluation of marine synthetic data. We use the first derivative of the Gaussian function with a maximum frequency of 10 Hz to generate the source wavelet. Figs. 2a and 2b are the P- and S-wave velocities of the Hess model, respectively, and Fig. 2c is the density. We assume a 300-channel hydrophone streamer recording pressure data over a grid of 20 m unit cells, with a source firing 385 shots at 40 m intervals and at typical marine seismic survey depths. The recording time is 12 s. Fig. 3 shows the 151st-155th shot data, as generated and extracted from synthetic data via staggered grid time modeling. When performing reverse time migration, we assumed that the true P- and S-wave velocities and density values are known. We performed frequency domain reverse time migration for acoustic and acoustic-elastic coupled media using the conventional zero-lag cross-correlation method [eqs. (16) and (17)] and the wavefield separation method [eqs. (18) and (19)] for comparison. Fig. 4 shows the migration image of the acoustic-based frequency domain reverse time migration. Figs. 5a and 5b show the migration images of the P- and S-wave velocities, respectively, which were calculated via the frequency domain reverse time migration for acoustic-elastic coupled media using the conventional zero-lag cross-correlation method. The comparison between the migration images of the acoustic based algorithm (Fig. 4) and the P-wave image from the reverse time migration for acoustic-elastic coupled media (Fig. 5a) demonstrates that the reverse time migration image of acoustic-elastic coupled media can resolve more detailed geologic structures, such as specific sediment layers and the boundary of the salt body, than the migration image generated by the acoustic-based algorithm. In addition, the reverse time migration for acoustic-elastic coupled media can construct migration images of the S-wave velocity, although these images are of a lower quality than P-wave velocity images. We used the wavefield separation method to construct more high-resolution migrated images for acoustic-elastic coupled media. Figs. 6a and 6b show the migration images of the frequency domain reverse time migration for acoustic-elastic coupled media using the wavefield separation method. Fig. 6a shows the migration image based on P-wave velocity from a decomposed wavefield, as computed using the divergence operation, while Fig. 6b shows a migration image based on S-wave velocity from a decomposed wavefield, as computed using the curl operation.
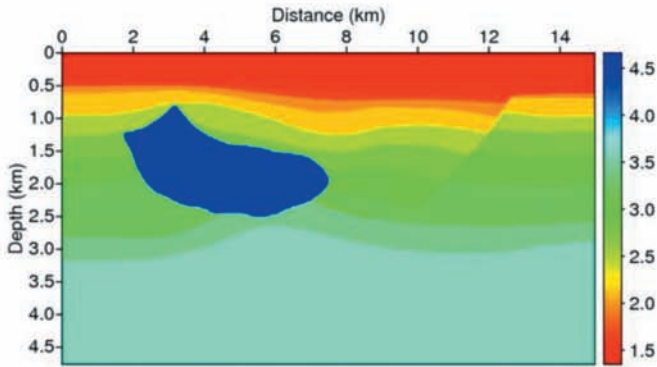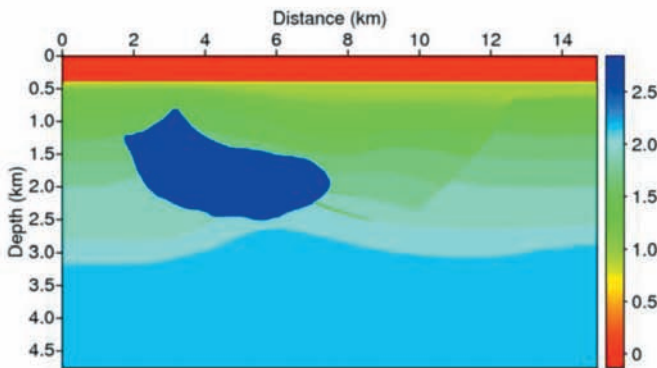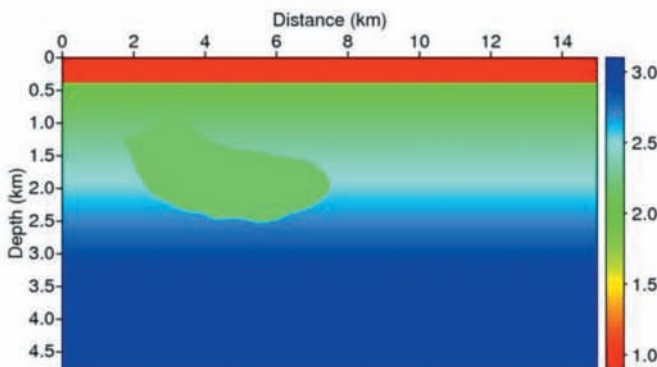
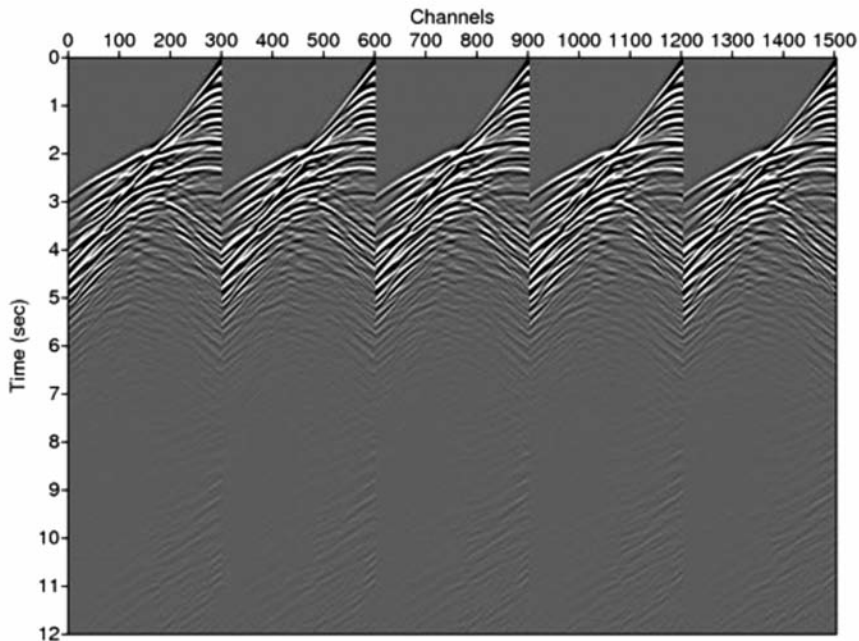Fig. 2. Hess model: (a) P-wave velocity, (b) S-wave velocity and (c) density.

Fig. 3. Synthetic Hess model data that were generated by a staggered grid modeling algorithm in the time domain (151st-155th shot gathers).
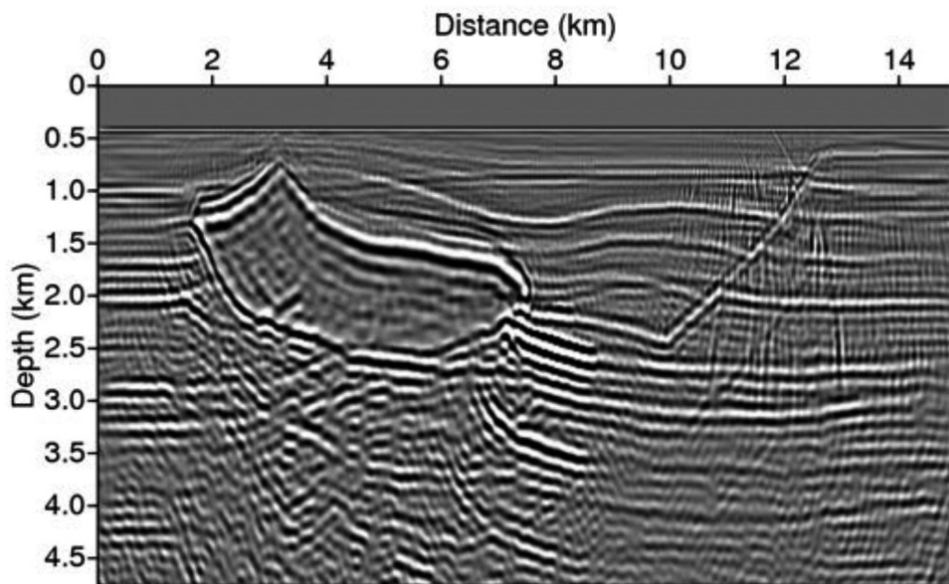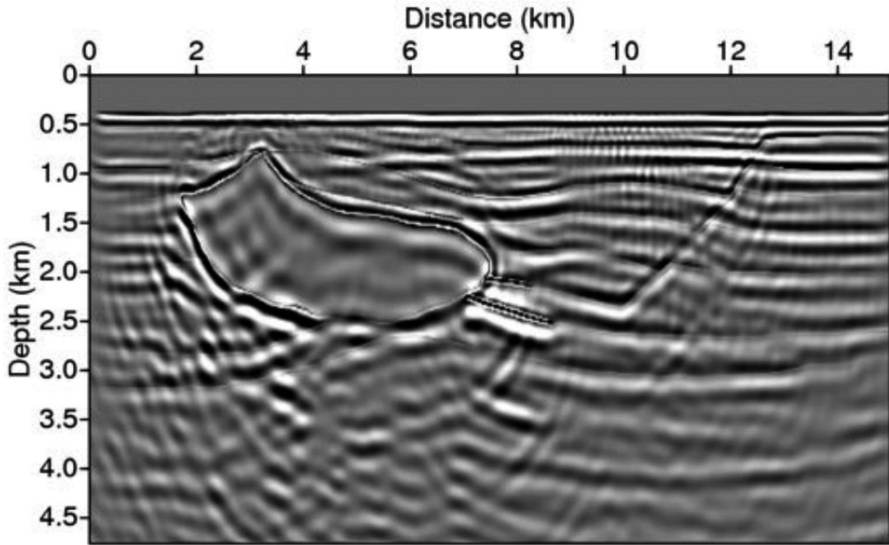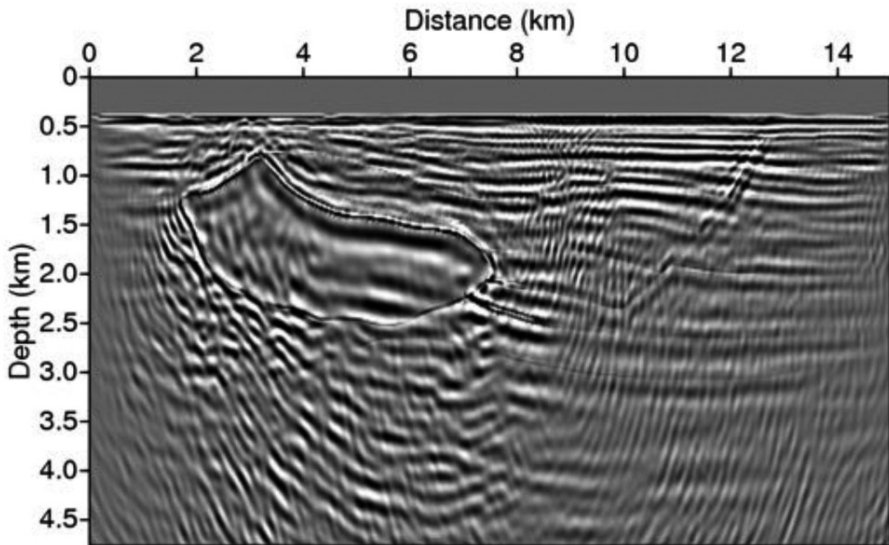

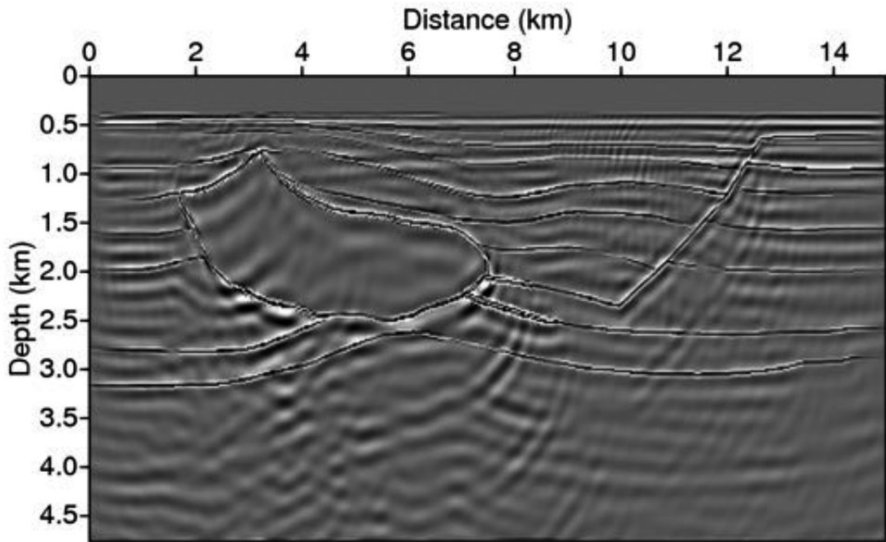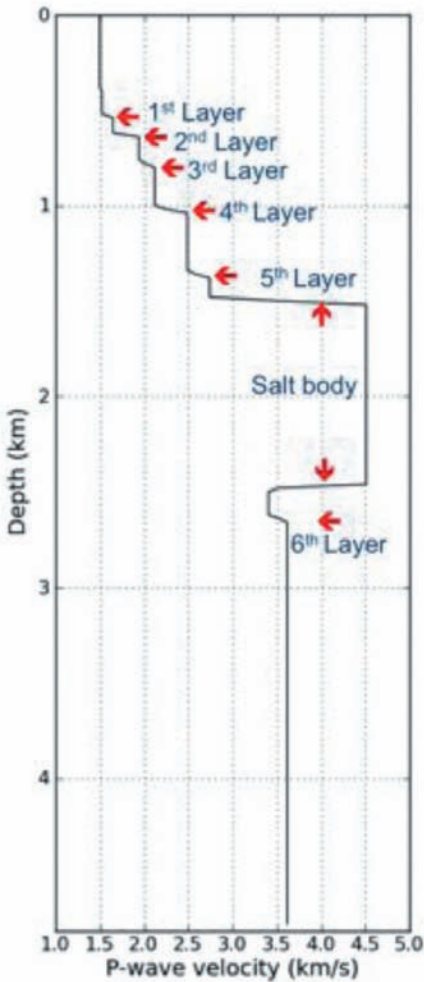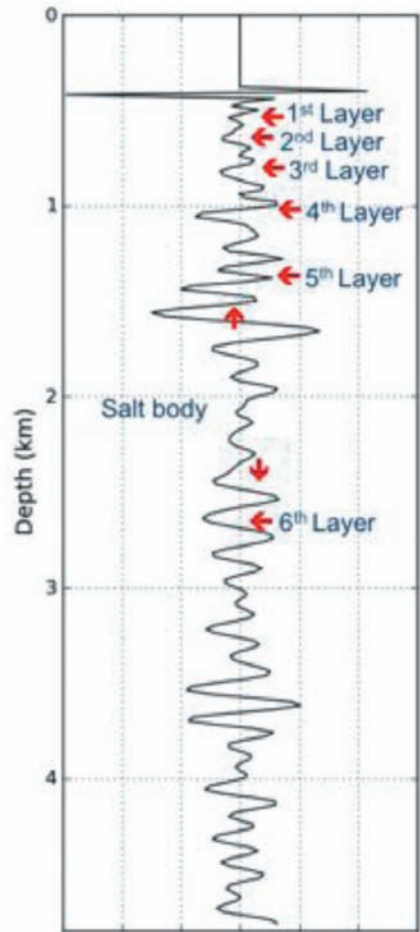Fig. 4. Migrated image of the Hess model via acoustic-based frequency domain reverse time migration.

(a)

(b)

Fig. 5. Migrated images of the Hess model via the frequency domain reverse time migration for acoustic-elastic coupled media using the conventional zero-lag cross-correlation method: (a) P-wave migration image and (b) S-wave migration image.

(a)
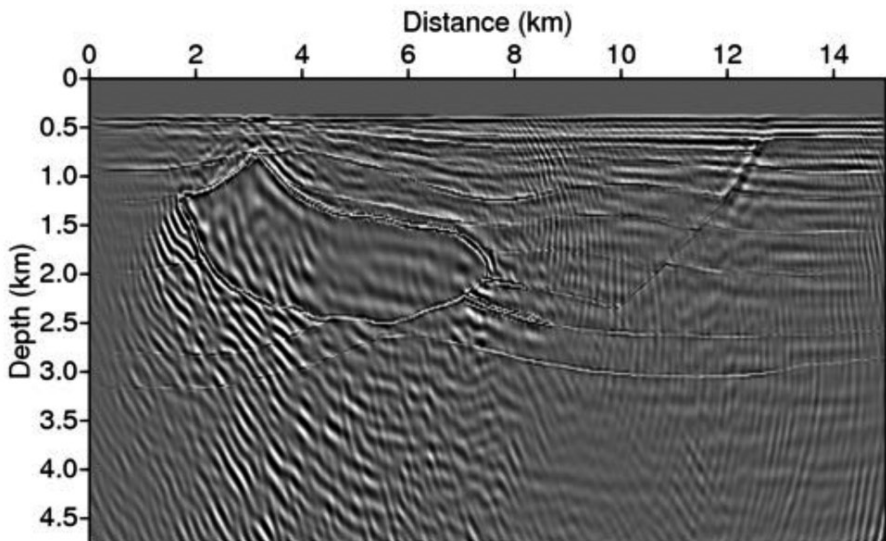
(b)

Fig. 6. Migrated images of the Hess model via the frequency domain reverse time migration for acoustic-elastic coupled media using the wavefield separation method: (a) P-wave migration image and (b) S-wave migration image.

Comparison of these migration images with those rendered by the conventional method (Fig. 5), shows that the wavefield separation method represents geologic structure with greater sharpness and more detail. The lower part of a salt body, sediment layers and fault boundaries are especially well defined in the images calculated using the wavefield separation method. The migration image based on wavefield separation and S-wave velocity shows a more resolved salt dome boundary and sediment layers than the image generated by conventional method. For a more detailed comparison, we examine the depth profiles of the true P-wave velocity and each of the migration images in Fig. 7.

(a)   (b)
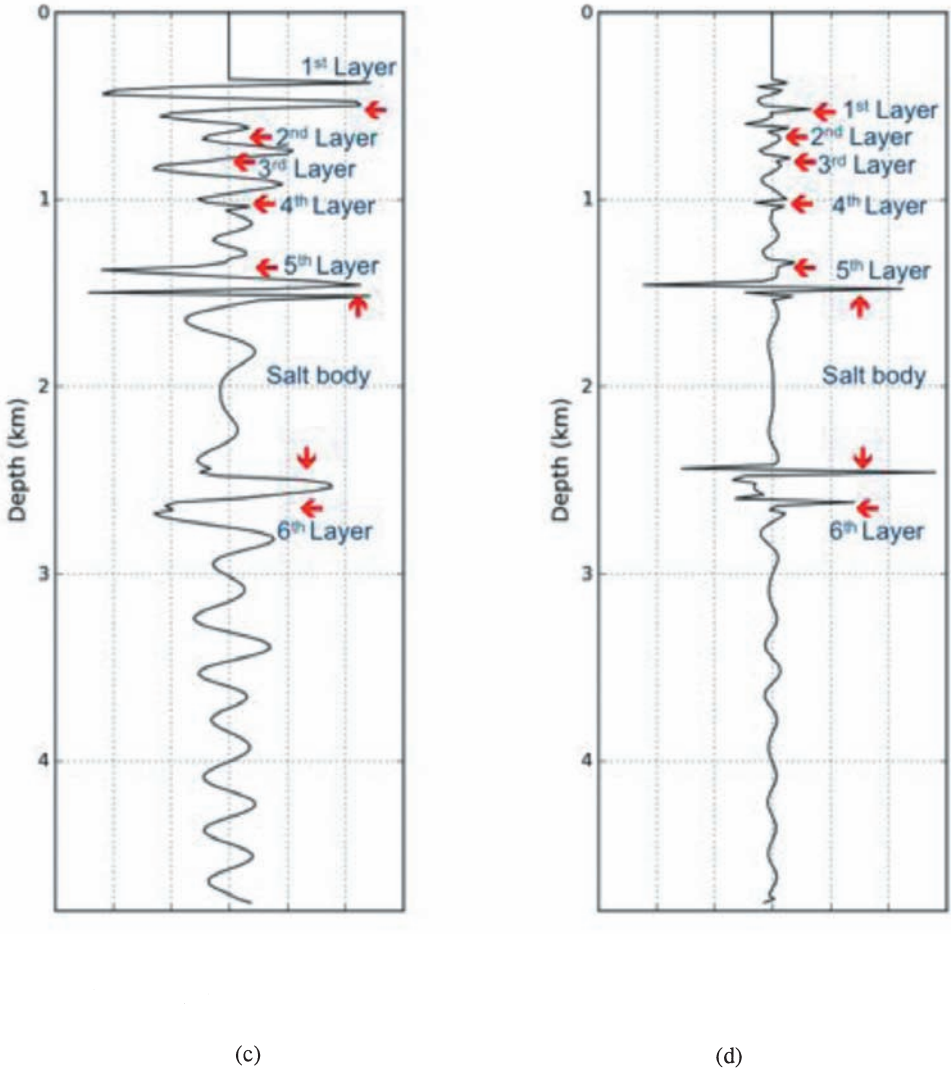
Fig. 7. Depth profile of the Hess model and the migrated images: (a) depth-true P-wave velocity profile, (b) depth-migrated image of the acoustic-based frequency domain reverse time migration, (c) depth-migrated image of the frequency domain reverse time migration for acoustic-elastic coupled media using the conventional zero-lag cross-correlation method and (d) depth-migrated image of the frequency domain reverse time migration for acoustic-elastic coupled media using the wavefield separation method.

Fig. 7a depicts the depth-true P-wave velocity profile at 6 km, as extracted from Fig. 2a. Figs. 7b, 7c and 7d show the depth-migrated profiles at 6 km as calculated from migration images based on the acoustic-based algorithm (Fig. 4), the acoustic-elastic coupled media from the conventional zero-lag cross-correlation method (Fig. 5a) and the wavefield separation method (Fig. 6a). Fig. 7a specifically notes geological structures detected from P-wave velocities (1st-6th sediment layers and salt boundaries) for comparison among the different migration image profiles. The migration image based on P-wave velocity from the frequency domain reverse time migration for acoustic-elastic coupled media using the wavefield separation method (Fig. 7d) consists of more discrete imaging components and shows sedimentary features from 0.5 km to 1 km and the salt dome boundary from 1.5 km to 2.5 km more clearly than images generated by the acoustic-based algorithm and the conventional zero-lag cross-correlation method. The 6th geological layer beneath the salt body was also well defined in images generated by the wavefield separation method but not in those generated by the other two methods. Comparison of the migration images and the depth-migrated profiles shows that the frequency domain reverse time migration for acoustic-elastic coupled media can render geologic structures in greater detail than the acoustic-based algorithm and requires a wavefield separation method to construct accurate migration images.
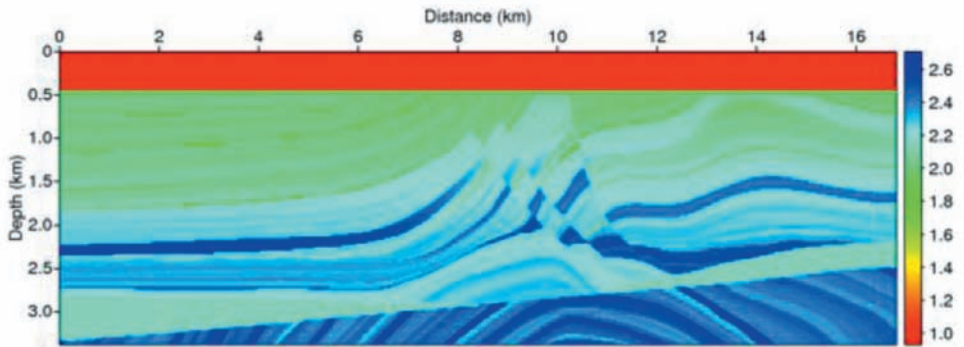
We also calculated migration images using the IFP/UH Marmousi-2 model (Martin et al., 2002), which includes various geological structures such as shale, faults, a sand layer charged with natural gas, an unconformity, a gas and oil cap along the bottom part of the model, and other features. Fig. 8 shows the IFP/UH Marmousi-2 model assuming a water depth of 500 m. For this migration test, we generated synthetic marine data using staggered grid modeling based on the first-order elastic wave equation. The source wavelet is the first derivative of the Gaussian function with a maximum frequency of 15 Hz. We assumed a 600-channel streamer to record data within a grid with a 10 m unit cell, and 802 shots at 20 m intervals discharged beneath the water's surface. The recording time is 12 s. Fig. 9 shows five shot gathers (301st-305th), which were extracted from the synthetic data. First, we conduct the migration test using the true P- and S-wave velocities and the density input models following the previous Hess model case. Fig. 10 shows the migration image of the acoustic-based algorithm. Figs. 11a and 11b show the migrated images based on P- and S-wave velocities (respectively) from the reverse time migration for acoustic-elastic coupled media using the conventional zero-lag cross-correlation method. Figs. 12a and 12b show the migrated images based on P- and S-wave velocities as calculated from the reverse time migration for acoustic-elastic coupled media using the wavefield separation method. The migration image based on P-wave velocity from the acoustic algorithm (Fig. 10) reveals the location and shape of an anticline, but offers only limited resolution for the interior of the anticline. However, the migration image based on P-wave velocity (Fig. 11a) according to the reverse time migration of acoustic-elastic
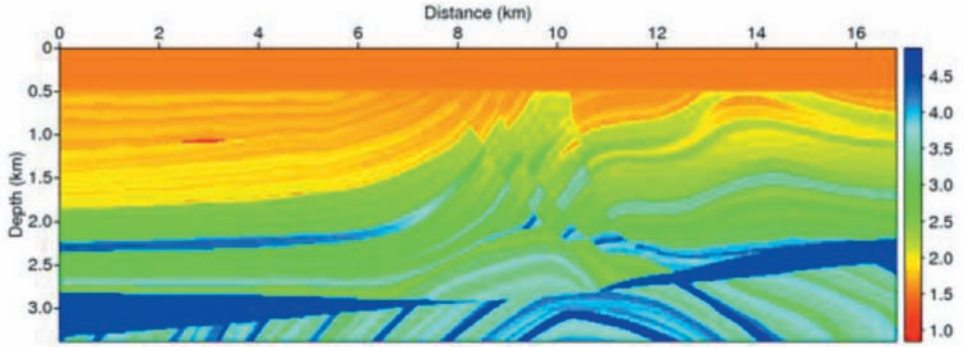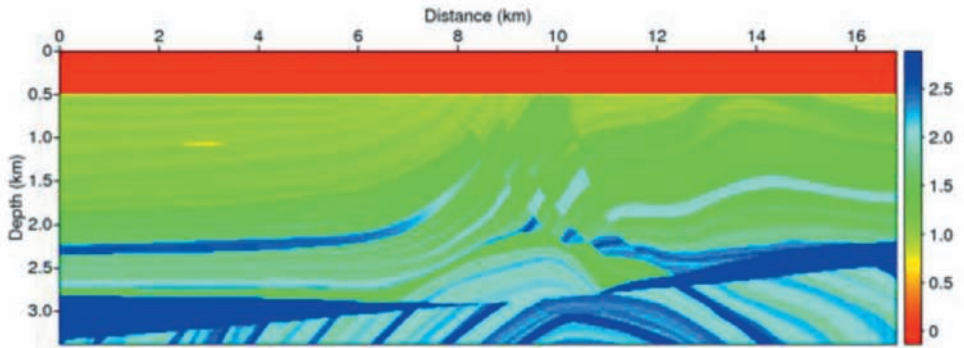
Fig. 8. IFP/UH Marmousi-2 model: (a) P-wave velocity, (b) S-wave velocity and (c) density.

coupled media using the conventional zero-lag cross-correlation method resolves the interior of the anticline in greater detail compared to the migration image from acoustic reverse time migration. The migration image based on the P-wave velocity from the reverse time migration for acoustic-elastic coupled media using the wavefield separation method (Fig. 12a) represents the anticline in greater detail and with sharper lines indicating sedimentary layers, as compared to the migration image generated by the conventional acoustic-elastic coupled method (Fig. 11a). Although the migrated S-wave image is not as accurate as the P-wave image, the wavefield separation method constructs better S-wave migration images (Fig. 12b) than the conventional algorithm (Fig. 11b). Fig. 13 shows depth profiles for the true P-wave velocity and each migrated P-wave image at 10.8 km. Fig. 13a shows the depth-true P-wave velocity profile, Figs. 13b, 13c and 13d depict the depth-migrated image profiles based on migrated images of the acoustic-based algorithm (Fig. 10), the conventional acoustic-elastic coupled algorithm (Fig. 11a) and the wavefield separation method (Fig. 12a), respectively. Compared with the profile from the true model,
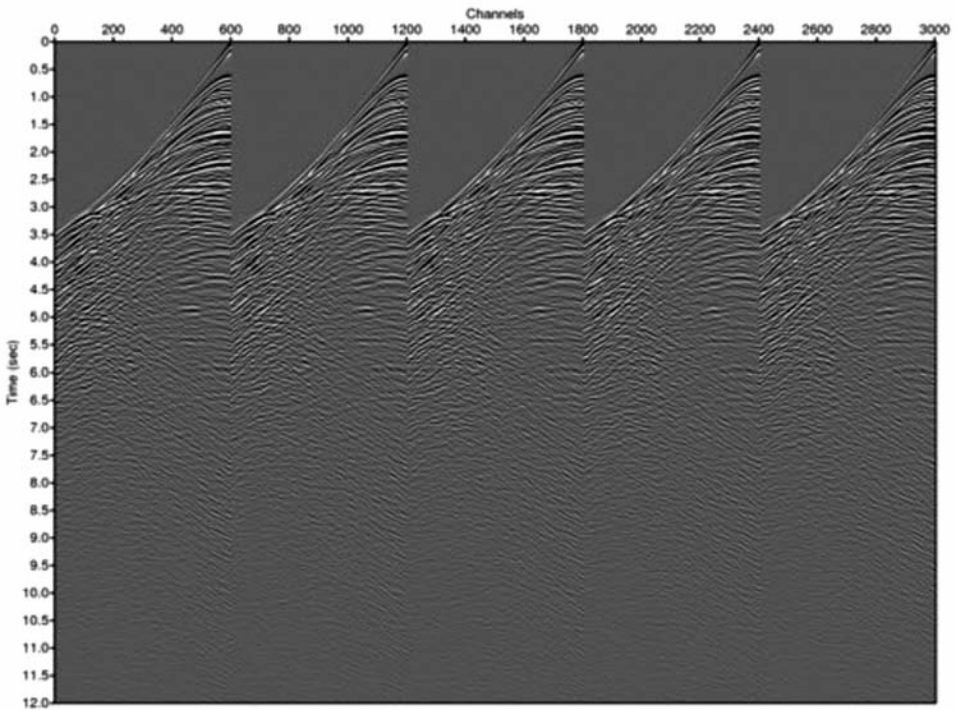

Fig. 9. Synthetic IFP/UH Marmousi-2 model data generated by a staggered grid algorithm (301st-305th shot gathers).
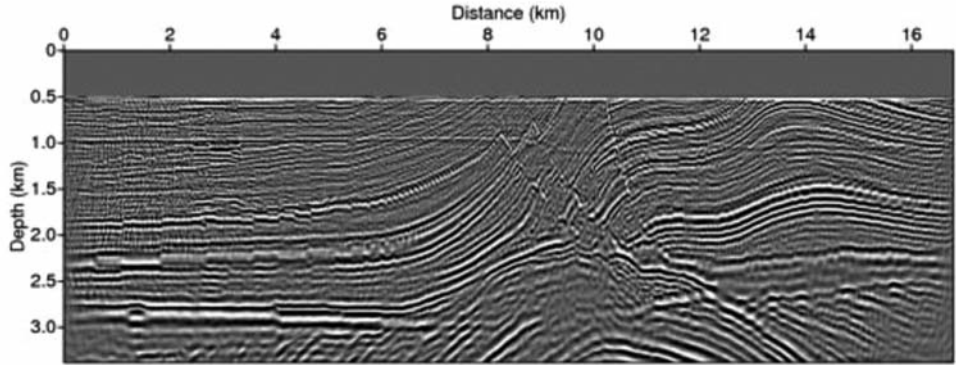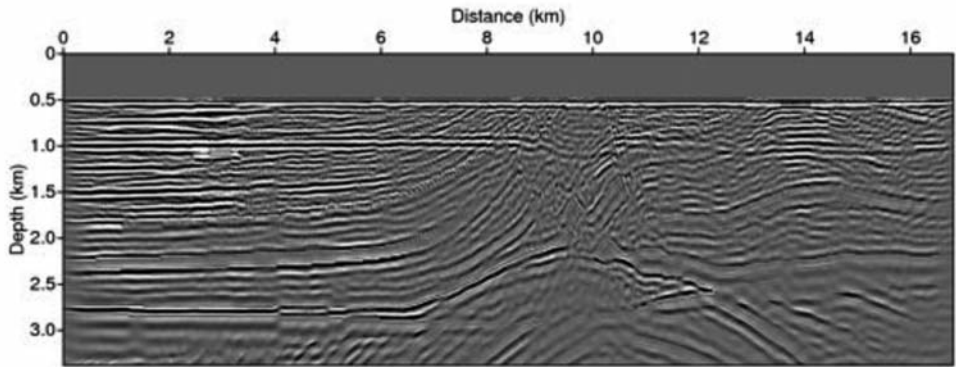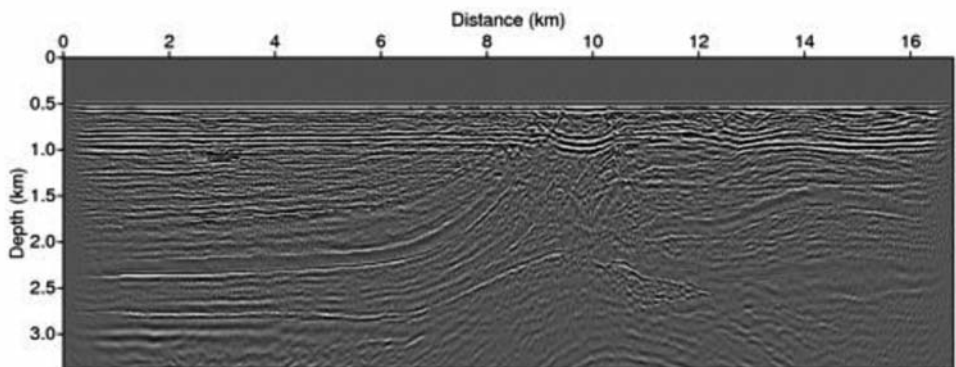
Fig. 10. Migrated image of the IFP/UH Marmousi-2 model via acoustic-based frequency domain reverse time migration.
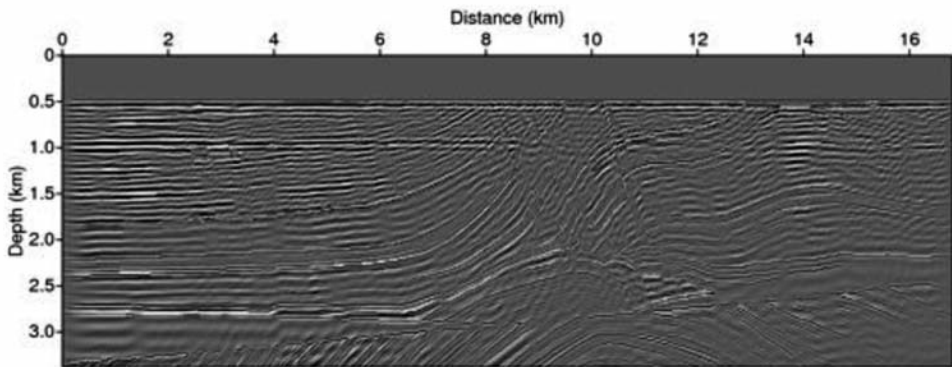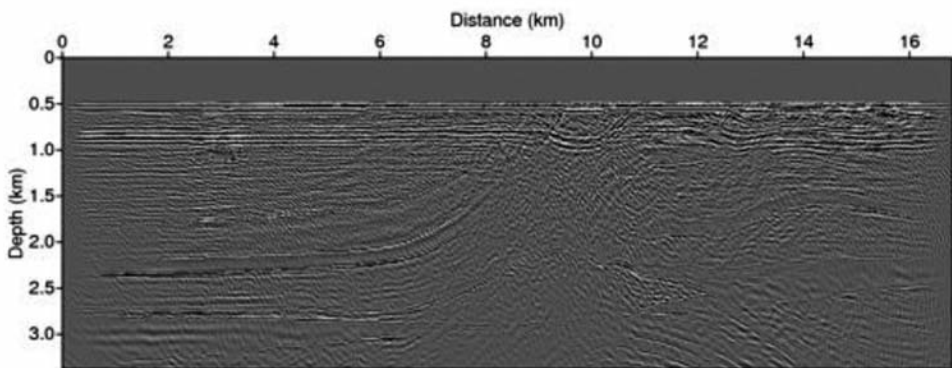

(a)

(b)

Fig. 11. Migrated image of the IFP/UH Marmousi-2 model via the frequency domain reverse time migration for acoustic-elastic coupled media using the conventional zero-lag cross-correlation method: (a) P-wave migration image and (b) S-wave migration image.

upper geologic structures (1st and 2nd layers) are well defined in the image calculated from reverse time migration for acoustic-elastic coupled media using the conventional zero-lag cross-correlation method and the wavefield separation method. The acoustic-based reverse time migration method however does not reveal accurate geologic structures in the upper parts of the target model. In addition, the acoustic image also does not render the substructure below 2 km depth (3rd-7th layers). The P-wave image of the acoustic-elastic coupled media from the conventional algorithm does not clearly show the substructure below 2.5 km (5th-7th layers) in the depth-migration image profile because the image consists of low values at boundaries of geologic structures. The depth-migration image profile of the acoustic-elastic coupled media from the wavefield separation technique (Fig. 13d) however, accurately describes the positions of the subsurface geologic structures with more discrete signal events for the entire target model.
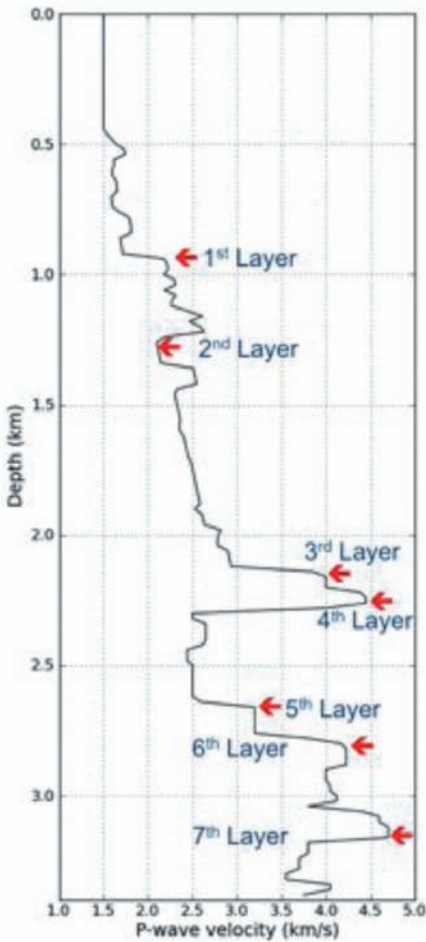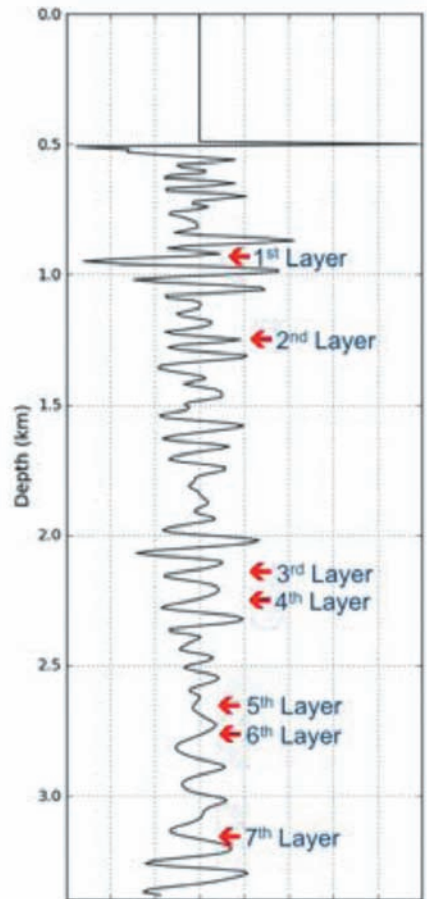

(a)

(b)

Fig. 12. Migrated image of the IFP/UH Marmousi-2 model via the frequency domain reverse time migration for acoustic-elastic coupled media using the wavefield separation method: (a) P-wave migration image and (b) S-wave migration image.

   We performed migration tests for 2 types of synthetic data, which were generated via staggered grid time modeling with the Hess and IFP/UH Marmousi-2 models. The frequency domain reverse time migration for acoustic-elastic coupled media could then reconstruct geological structures with greater accuracy compared to the acoustic-based migration algorithm, especially for deeper areas of the target model. We furthermore confirmed that the wavefield separation method is necessary to calculate the migration image for acoustic-elastic coupled media.

(a)

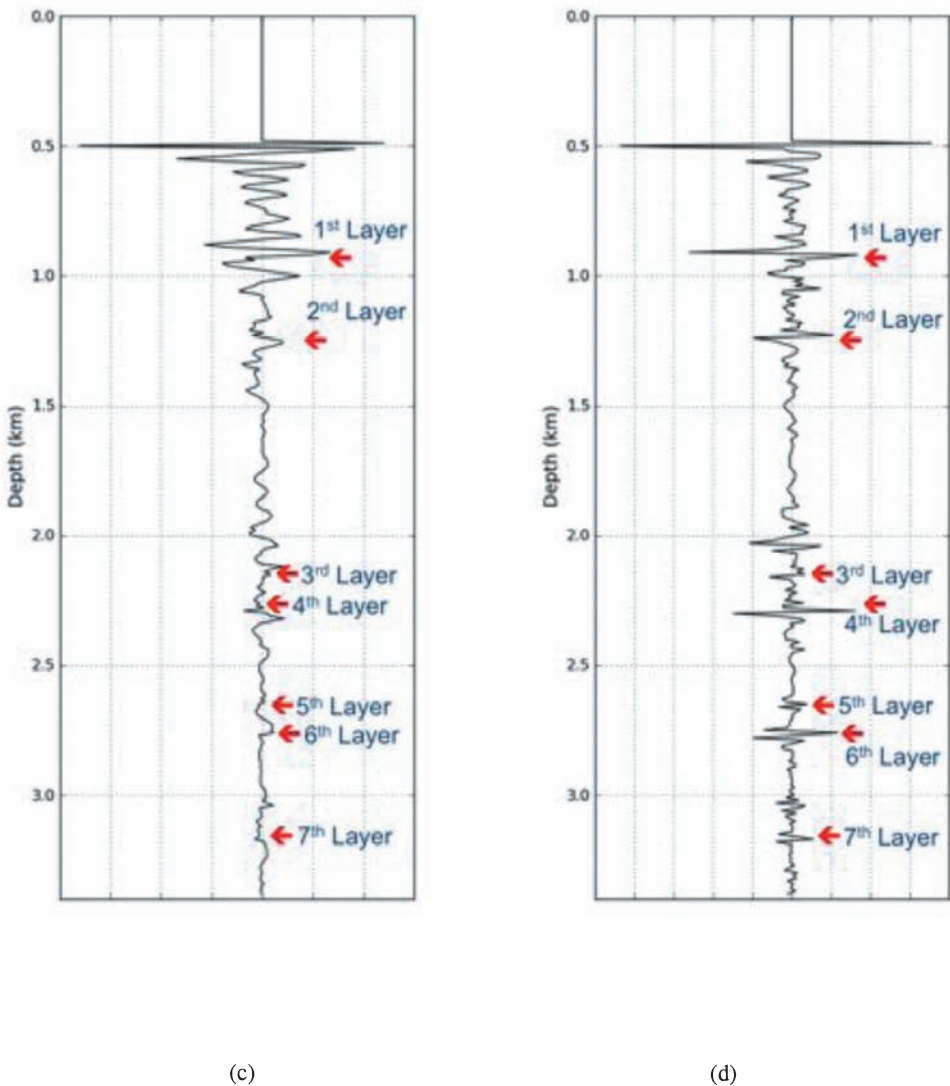(b)

(c)   (d)

Fig. 13. Depth profile of the IFP/UH Marmousi-2 model and the migrated images: (a) depth-true P-wave velocity profile, (b) depth-migrated image of the acoustic-based frequency domain reverse time migration, (c) depth-migrated image of the frequency domain reverse time migration for acoustic-elastic coupled media using the conventional zero-lag cross-correlation method and (d) depth-migrated image of the frequency domain reverse time migration for acoustic-elastic coupled media using the wavefield separation method.
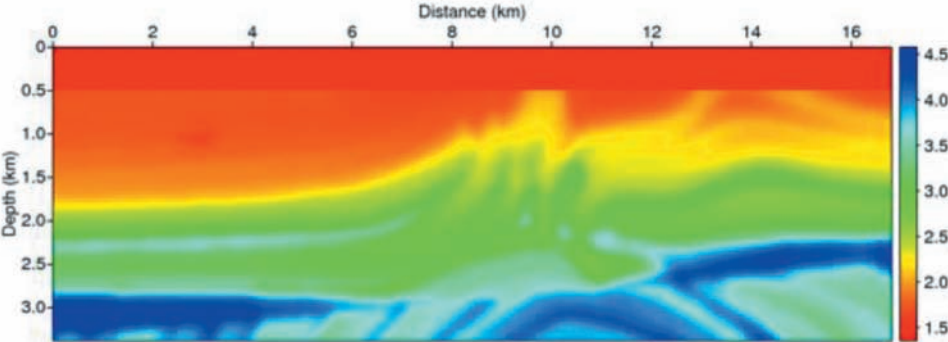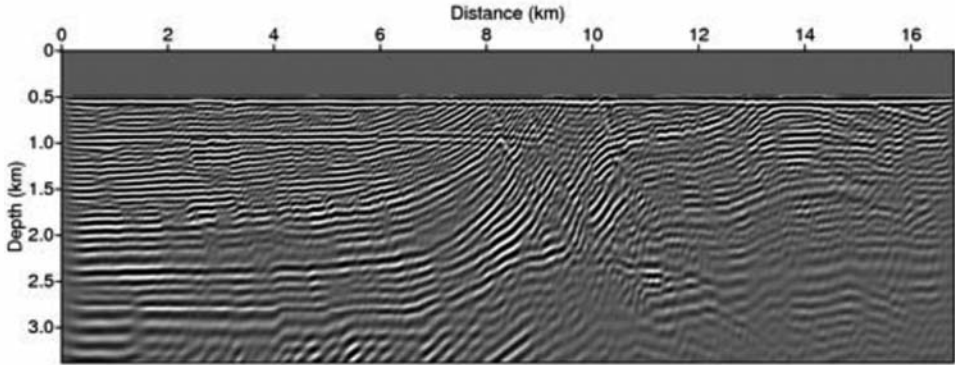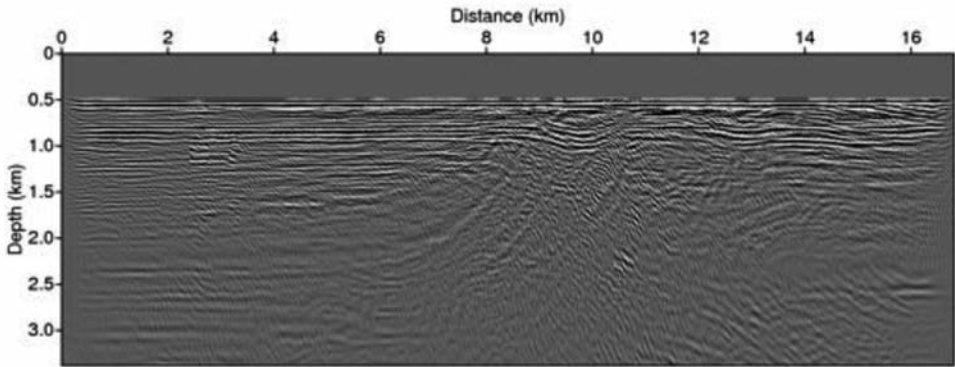
(a)
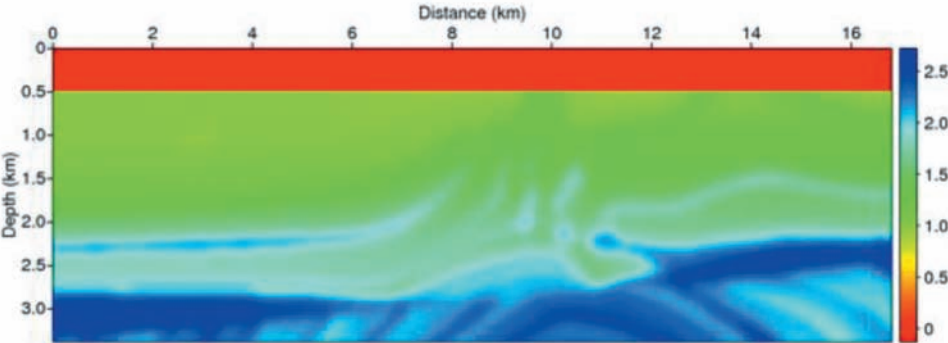
(b)
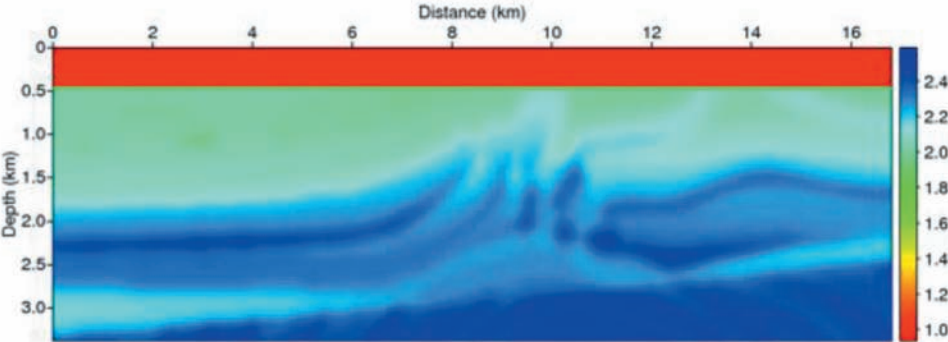
(c)

Fig. 14. Smoothed IFP/UH Marmousi-2 models (smoothing parameter = 20). (a) P-wave velocity, (b) S-wave velocity and (c) density.

Fig. 15. Migrated image of the smoothed P- and S-wave velocity and density models via the frequency domain reverse time migration for acoustic-elastic coupled media using the wavefield separation method: (a) P-wave migration image and (b) S-wave migration image.

We also performed additional migration tests with IFP/UH Marmousi-2 synthetic data to examine the sensitivity of results to the input models for acoustic-elastic coupled media. For these tests, we used IFP/UH Marmousi-2 models smoothed using the Seismic Unix software system's smooth2 function, set with a smoothing parameter of 20 (Fig. 14). Figs. 15a and 15b show migrated images from the reverse time migration for acoustic-elastic coupled media using all smoothed input models. Figs. 16a and 16b show the migrated images of the reverse time migration for acoustic-elastic coupled media using the true P-wave velocity model with smoothed S-wave velocity and density models. Fig. 17 shows the migrated images of the reverse time migration for acoustic-elastic coupled media using the true S-wave velocity model with

smoothed P-wave and density models. Fig. 18 shows the migrated images of the reverse time migration for acoustic-elastic coupled media using the true density model with smoothed P- and S-wave velocity models. Comparison of the migration images (Figs. 15, 16, 17 and 18) shows that reverse time migration for acoustic-elastic coupled media requires accurate models for imaging. The P-wave velocity model is the most important factor in calculating migration images because migrated images, which are calculated from the true P-wave velocity with smoothed S-wave and density input models, provide the best migration image (Fig. 16). According to the migration images in Fig. 16, the accuracy of the P-wave velocity model affects the P- and the S-wave migration image. An accurate S-wave model does not improve the quality of the migration images (Fig. 17). An accurate density model does improve image quality but is inadequate and limited to the P-wave image (Fig. 18).
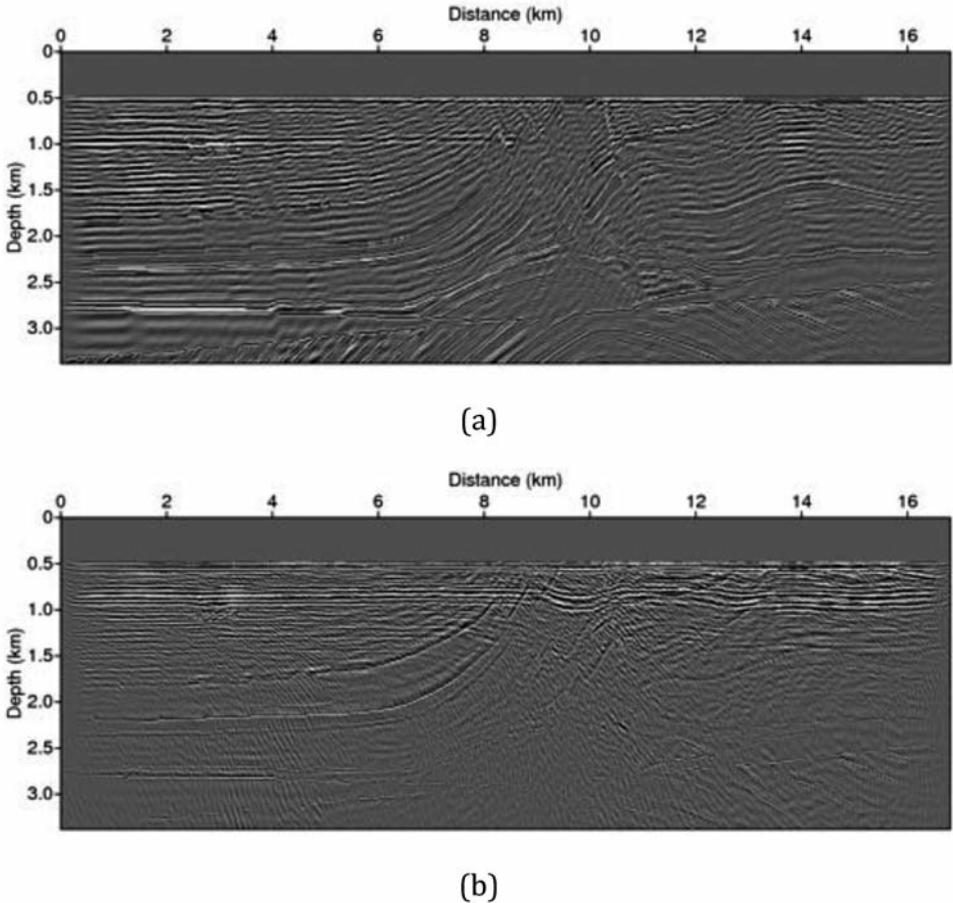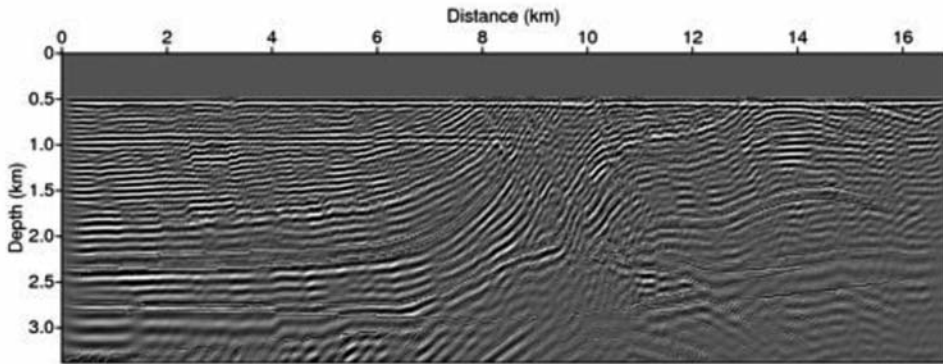

(a)

(b)

Fig. 16. Migrated image of the true P-wave velocity and smoothed S-wave velocity and density models via the frequency domain reverse time migration for acoustic-elastic coupled media using the wavefield separation method: (a) P-wave migration image and (b) S-wave migration image.
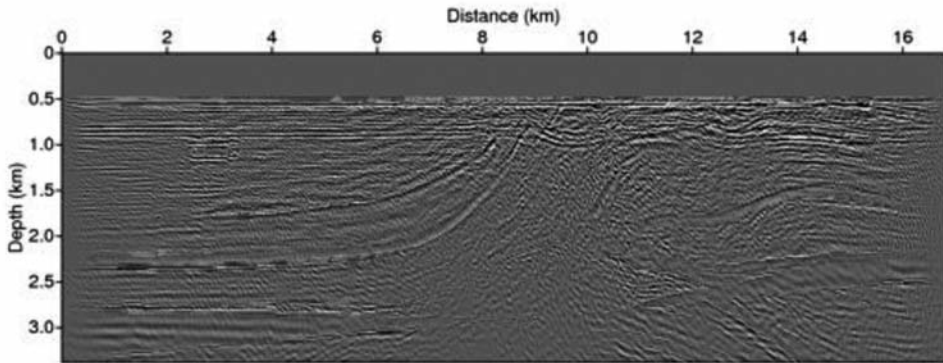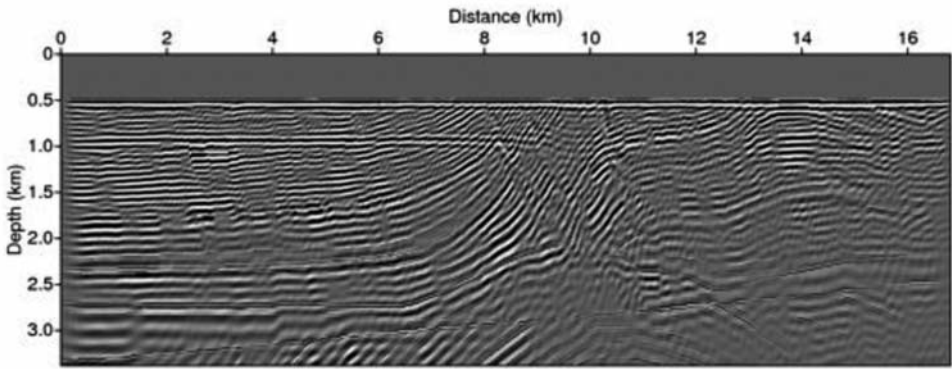
(a)

(b)

Fig. 17. Migrated image of the true S-wave velocity and smoothed P-wave velocity and density models via the frequency domain reverse time migration for acoustic-elastic coupled media using the wavefield separation method: (a) P-wave migration image and (b) S-wave migration image.

CONCLUSIONS

We described a reverse time migration for acoustic-elastic coupled media in the frequency domain to examine elastic wave effects in marine seismic data, including shear reflections and mode-converted waves. Reverse time migration was used to generate both P- and S-wave images, in keeping with methods for full waveform inversion of acoustic-elastic coupled media. We then applied a wavefield separation method based on the decomposed wavefield, which was used in the elastic medium to improve the fidelity of the migrated image. We

compared the results of our migration algorithm for acoustic-elastic coupled media that used the wavefield separation method to images generated by the conventional zero-lag cross-correlation method and the acoustic approach using synthetic datasets that were generated by elastic staggered grid time-domain modeling. The numerical results demonstrated the applicability of the wavefield separation method for use in acoustic-elastic coupled media and for generating P-wave migration images more accurate than those generated by the acoustic migration algorithm.

(a)

(b)

Fig. 18. Migrated image of the true density and smoothed P- and S-wave velocity models via the frequency domain reverse time migration for acoustic-elastic coupled media using the wavefield separation method: (a) P-wave migration image and (b) S-wave migration image.
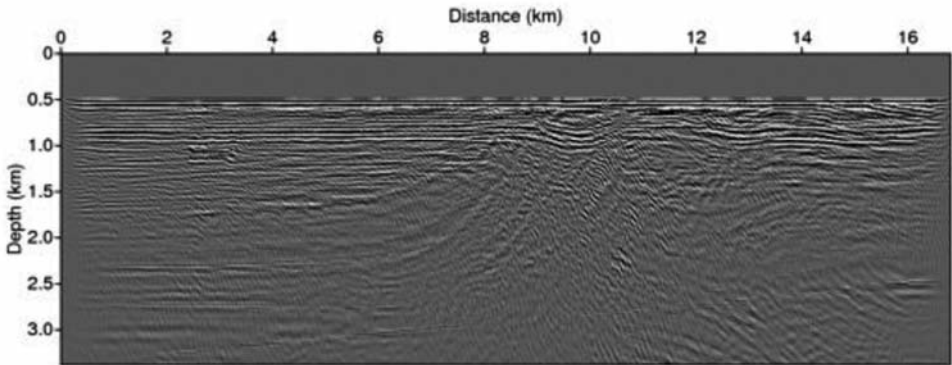
For a more detailed comparison, we examined the depth profiles of the true velocity for each type of migration image. The depth-migration image profiling of acoustic-elastic coupled media from the wavefield separation technique accurately detected the position of subsurface geologic structures with discrete signal events throughout the entire target model. These numerical tests show that the frequency domain reverse time migration for acoustic-elastic coupled media can more accurately image geologic structures than the acoustic-based migration algorithm, especially in deeper areas of the target model. The wavefield separation method plays an important role in generating migration images from acoustic-elastic coupled media.

We also examined the images' sensitivity to the subsurface models using the IFP/UH Marmousi-2 model. The results demonstrated that a correct P-wave velocity model is more important than a correct S-wave velocity. Reverse time migration images for acoustic-elastic coupled media strongly depend on accurate density estimates.

The frequency domain reverse time migration for acoustic-elastic coupled media with wavefield separation method can be used in prestack depth migration for field data. Future studies will focus on the application of our reverse time migration to field data from extreme environments, such as Antarctic region, Arctic permafrost, and containing steep reflectors or sudden seismic velocity variation.

ACKNOWLEDGEMENTS

REFERENCES

Bae, H.S., Shin, C., Cha, Y.H., Choi, Y. and Min, D., 2010. 2D acoustic-elastic coupled waveform inversion in the LaPlace domain. Geophys. Prosp., 58: 997-1010.
Baysal, E., Kosloff, D.D. and Sherwood, J.W.C., 1983. Reverse time migration. Geophysics, 48: 1514-1524.
Choi, Y., Min, D.-J. and Shin, C., 2008. Two-dimensional waveform in- version of multicomponent data in acoustic-elastic coupled media. Geophysics, 56: 863-881.
Chung, W., Pyun, S., Bae, H.S., Shin, C. and Marfurt, K.J., 2012. Implementation of elastic reverse-time migration using wavefield separation in the frequency domain. Geophys. J. Int., 189: 1611-1625.
Cohen, G.C., 2002. High-Order Numerical Methods for Transient Wave Equations. Springer Verlag, Berlin.
Kang, S.-G., Bae H.S. and Shin, C., 2012. Laplace-fourier-domain waveform inversion for fluid-solid media. Pure Appl. Geophys., 169: 2165-2179.

Kim, M.H., Choi, Y., Cha, Y.H. and Shin, C., 2009. 2-D frequency-domain waveform inversion of coupled acoustic-elastic media with an irregular interface. Pure Appl. Geophys., 166: 1967-1985.

Kim, Y., Min, D. and Shin, C., 2011. Frequency-domain reverse-time migration with source estimation. Geophysics, 76: S41-S49.

Komatitsch, D., Barnes, C. and Tromp, J., 2000. Wave propagation near a fluid-solid interface: A spectral-element approach. Geophysics, 65: 623-631.

Lailly, P., 1983. The seismic inverse problem as a sequence of before stack migrations. Expanded Abstr., Conf. Inverse Scattering: Theory and Application Mathematics: 206-220.

Lee, H., Lim, S., Min, D., Kwon, B. and Park, M., 2009. 2D time-domain acoustic-elastic coupled modeling: a cell-based finite-difference method. Geosci. J., 13: 407-414.

Lee, J., Kim, Y. and Shin, C., 2012. Frequency-domain reverse time migration using the L_1-norm. J. Seismic Explor., 21: 281-300.

Loewenthal, D. and Mufti, I.R., 1983. Reversed time migration in spatial frequency domain. Geophysics, 48: 627-635.

Martin, G.S., Marfurt, K.J. and Larsen, S. 2002. Marmousi-2: an updated model for the investigation of AVO in structurally complex areas. Expanded Abstr., 72nd Ann. Internat. SEG Mtg., Salt Lake City: 1979-1982.

McMechan, G.A., 1983. Migration by extrapolation of time-dependent boundary values. Geophys. Prosp., 31: 413-420.

Plessix, R.-E. and Mulder, W.A., 2004. Frequency-domain finite-difference amplitude preserving migration. Geophys. J. Internat., 157: 975-987.

Pratt, R.G., Shin, C. and Hicks, G.J., 1998. Gauss-Newton and full Newton method in frequency domain seismic waveform inversion. Geophys. J. Internat., 133: 341-362.

Shin, C., Jang, S. and Min, D., 2001. Improved amplitude preservation for prestack depth migration by inverse scattering theory. Geophys. Prosp., 49: 592-606.

Shin, C., Min, D.J., Yang, D. and Lee, S.K., 2003. Evaluation of poststack migration in terms of virtual source and partial derivative wavefields. J. Seismic Explor., 12: 17-37.

Symons, N.P., Aldridge, D.F. and Haney, M.M., 2006. 3D acoustic and elastic modelling with Marmousi-2. Expanded Abstr., 76th Ann. Internat. SEG Mtg., New Orleans: 2171-2175.

Tarantola, A., 1984. Inversion of seismic reflection data in the acoustic approximation. Geophysics, 49: 1259-1266.

Virieux, J., 1986. P-SV wave propagation in heterogeneous media: velocity-stress finite-difference method. Geophysics, 51: 889-901.

Whitmore, N.D., 1983. Iterative depth migration by backward time propagation. Expanded Abstr., 53rd Ann. Internat. SEG Mtg., Las Vegas: 382-385.

Xu, K., Zhou, B. and McMechan, G.A., 2010. Implementation of prestack reverse time migration using frequency-domain extrapolation. Geophysics, 75: S61-S72.

Zienkiewicz, O.C., Taylor, R.L. and Zhu, J.Z., 2005. The Finite Element Method: Its Basis and Fundamentals. Elsevier, Butterworth-Heinemann, New York.